Journal of Computational Physics 394 (2019) 1–17

Contents lists available at ScienceDirect

Journal of Computational Physics

www.elsevier.com/locate/jcp

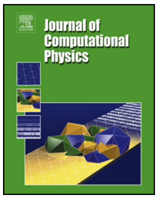

Vaporization of liquid droplet with large deformation and high mass transfer rate, II: Variable-density, variable-property case

Yanxing Wang [a], Xiaodong Chen [b], Xingjian Wang [a], Vigor Yang [a,*]

[a] School of Aerospace Engineering, Georgia Institute of Technology, Atlanta, GA 30332, USA
[b] School of Aerospace Engineering, Beijing Institute of Technology, Beijing, 100081, China

ARTICLE INFO

Article history:
Received 23 August 2017
Received in revised form 23 April 2019
Accepted 25 April 2019
Available online 6 May 2019

Keywords:
Liquid vaporization
Droplet deformation
Variable density

ABSTRACT

A novel approach for treating vaporization of liquid droplets with large deformation and high mass transfer rate is developed. The formulation is based on decomposed vaporization mechanisms and accommodates the effects of density and property variations in both the gas and liquid phases. In this model, the mass and energy transfer across the interface are realized by a source layer in the gas phase and a sink layer in the liquid phase around the interface. The flow field in each phase is described by a set of unified conservation equations in the low Mach number limit. The equations are then solved by a modified projection method, in which the nonzero velocity divergence is treated as a source term in the pressure Poisson equation. The vaporization model is implemented in a volume-of-fluid (VOF) based code "Gerris" featuring adaptive mesh refinement. The vaporization of a single *n*-decane droplet in both quiescent and convective air environments of 1000 K at 1 atm is investigated to verify and validate the present model in terms of interface localization and mass conservation. The results demonstrate the accuracy and robustness of the present work. The vaporization of an impulsively started *n*-decane droplet with large deformation and breakup is also studied. The droplet surface dynamics are captured well, as are the vaporization behaviors.

1. Introduction

In Ref. [1], we developed a new model dealing with vaporization of a liquid droplet with large deformation and high mass transfer rate, based on decomposed treatment of vaporization mechanisms. In this model, the vaporization-related variations of volume, energy, and species in the gas phase are modeled using a body-fitted source layer adjacent to the interface on the gas side. A corresponding body-fitted sink layer is placed next to the interface on the liquid side, to account for the mass, energy, and species changes in the liquid phase. The source and sink terms have a continuous distribution and are specified through the conservation laws. The new model allows for the separate treatment of interface localization and heat and mass transfer across the interface. It has been demonstrated to effectively capture the liquid-gas interface, while substantially reducing the error and complexity introduced by concurrent treatment of surface localization and mass/heat transfer, as encountered in conventional interface localization methods [1].

Most vaporization models assume constant density for both liquid and gas phases, to bypass the difficulties associated with the coupling of two-phase flows. For a vaporization process with high mass transfer driven by a large temperature

---

[*] Corresponding author.
E-mail address: vigor.yang@aerospace.gatech.edu (V. Yang).

https://doi.org/10.1016/j.jcp.2019.04.052

difference, however, gas-phase properties such as density, viscosity, and thermal conductivity change significantly near the interface, because of the variation of temperature and species concentration. When the initial liquid temperature is significantly lower than the boiling temperature, the heating process causes non-negligible property variation and thermal expansion in the liquid phase, although the relative density change of the liquid is smaller than that of the gases. Therefore, neglecting property variation and treating the fluid as constant-density may cause considerable errors in prediction.

There are generally three different types of approaches to liquid vaporization: constant density in both phases, variable density in both phases, and constant density in the liquid phase but variable density in the gas phase. The first approach has been most broadly employed in vaporization models [1–5], as it provides the simplest way (also assuming constant properties in both phases) to study the problem. In the second approach, both gas and liquid phases are described by the conservation equations for variable-density flows, but with a different equation of state for each phase [6–11]. A major difficulty of such treatment lies in the disparity of the characteristic velocities of the flow field at low Mach numbers and the resultant numerical stiffness for time-marching iterations. To circumvent this difficulty, several techniques have been developed. Hsieh and Yang [12] and Meng and Yang [13], for example, developed a unified dual-time scheme with preconditioning to remedy eigenvalue disparity. The third type of models of liquid vaporization treats gas as compressible and liquid as incompressible [14]. It takes advantage of the phase decomposition techniques, such as the ghost fluid method, which couples the high-order scheme for the compressible flow with a standard scheme for the incompressible counterpart. This treatment retains the compressible nature of the gas phase and preserves numerical accuracy in each phase. Strictly speaking, this third class of model does not belong to the category of fully coupled treatment for two-phase flows. To this end, Billaud et al. [15] proposed a method based on a weak compressibility assumption in the gas phase to couple with the liquid phase; this model is capable of capturing the interface over a wide range of flow conditions.

In low-Mach number flows, the energy carried by acoustics is often unimportant to the overall solution, and the acoustic wavelength is usually much larger than the dimension of physical domain of interest. When flow motions are separated from acoustic waves, equations using low-Mach number approximation can be put in a form similar to that of the incompressible flow equations [16,17]. This motivates us to develop a unified coupling approach to accommodate the density variations in both gas and liquid phases.

In this paper, the vaporization model developed in Ref. [1] is extended to include the density variations in both the gas and liquid phases. The governing equations are numerically solved by a modified projection method [18,19], in which velocity divergence is treated as a source term in the pressure Poisson equation. Similarly, the effects of thermal expansion on temperature and species mass fractions are treated as the source terms in the energy and species equations, respectively. The resultant vaporization model is then incorporated into the volume-of-fluid (VOF)-based code “Gerris” [20,21]. As a demonstration example, the vaporization of a single n-decane droplet in both quiescent and convective air at room pressure is systematically investigated to examine the model accuracy and capability. Gerris is an open-source software program developed by Popinet [20,21] for incompressible single-phase and multi-phase fluid flows. The code employs an adaptive mesh projection method [22] to solve the time-dependent incompressible-flow equations, and uses the VOF approach to capture the gas-liquid interface in multi-phase flows. Here the flow compressibility (variable density) effect is accounted for by adding source terms in the governing equations to account for non-zero velocity divergence.

2. Mathematical formulation

The governing equations are based on the low Mach number approximation for compressible flows, which analytically filters out acoustic wave propagation while retaining compressibility effects associated with vaporization. At low Mach numbers, pressure can be decomposed into a thermodynamic component $p_0(t)$ that depends only on time and a perturbation component $p_g(\mathbf{x},t)$ that is on the order of magnitude of M^2, also known as gauge pressure [12,13]. The corresponding conservation equations of mass, momentum, energy, and species take the following form:

$$\frac{\partial \rho}{\partial t} + \nabla \cdot (\rho \mathbf{u}) = 0 \tag{1}$$

$$\frac{\partial (\rho \mathbf{u})}{\partial t} + \nabla \cdot (\rho \mathbf{u} \otimes \mathbf{u}) = -\nabla p_g + \nabla (\lambda \nabla \cdot \mathbf{u}) + \nabla \cdot (2\mu \mathbf{D}) + \sigma \kappa \delta_s \mathbf{n} \tag{2}$$

$$\frac{\partial (\rho h)}{\partial t} + \nabla \cdot (\rho h \mathbf{u}) = \nabla \cdot (k \nabla T) + \sum_k \nabla \cdot (\rho h_k D_k \nabla Y_k) + \sum_k q_k \dot{m}_k''' \tag{3}$$

$$\frac{\partial (\rho Y_k)}{\partial t} + \nabla \cdot (\rho Y_k \mathbf{u}) = \nabla \cdot (\rho D_k \nabla Y_k) + \dot{m}_k''' \tag{4}$$

where ρ is the density, $\mathbf{u}$ the velocity vector, Y_k the mass fraction of species k, h the enthalpy, T the temperature, and q_k and $\dot{m}_k'''$ the enthalpy and mass production rate of species k per unit volume due to vaporization, respectively. In the momentum equation, the surface tension is treated as a continuous body force expressed as $\sigma \kappa \delta_s \mathbf{n}$, where σ is the surface tension of the liquid in the gas, κ the interface curvature, and δ_s the Dirac-delta function. The velocity divergence relates to the volumetric source as

$$\nabla\cdot\mathbf{u}=S_v \tag{5}$$

where S_v is the volumetric source caused by thermal expansion and mass addition.

Substitution of the mass conservation equation (Eq. (1)) into the momentum equation (Eq. (2)) gives the non-conservative form of the momentum equation as

$$\rho\frac{\partial\mathbf{u}}{\partial t}+\rho\mathbf{u}\cdot\nabla\mathbf{u}=-\nabla p_g+\nabla(\lambda\nabla\cdot\mathbf{u})+\nabla\cdot(2\mu\mathbf{D})+\sigma\kappa\delta_s\mathbf{n} \tag{6}$$

Considering mass conservation, the energy equation (Eq. (3)) becomes

$$\frac{Dh}{Dt}=\frac{\partial h}{\partial t}+\mathbf{u}\cdot\nabla h=\frac{1}{\rho}\nabla\cdot(k\nabla T)+\frac{1}{\rho}\sum_k\nabla\cdot(\rho h_k D_k\nabla Y_k)+\frac{1}{\rho}\sum_k q_k\dot{m}_k''' \tag{7}$$

In the gas phase, the enthalpy of the gas mixture h is a function of temperature T, thermodynamic pressure p_0, and species mass fraction Y_k. The material derivative of enthalpy can be stated as

$$\frac{Dh}{Dt}=\left.\frac{\partial h}{\partial T}\right|_{p_0,Y_k}\frac{DT}{Dt}+\left.\frac{\partial h}{\partial p_0}\right|_{T,Y_k}\frac{Dp_0}{Dt}+\sum_k\left.\frac{\partial h}{\partial Y_k}\right|_{p_0,T,Y_{j,j\neq k}}\frac{DY_k}{Dt} \tag{8}$$

In the low Mach number limit, the thermodynamic component of pressure p_0 is constant. Substituting $Dp_0/Dt=0$ into Eq. (8), we have

$$\begin{aligned}\frac{Dh}{Dt}&=\left.\frac{\partial h}{\partial T}\right|_{p_0,Y_k}\frac{DT}{Dt}+\sum_k\left.\frac{\partial h}{\partial Y_k}\right|_{p_0,T,Y_{j,j\neq k}}\frac{DY_k}{Dt}\\&=\frac{1}{\rho}\nabla\cdot(k\nabla T)+\frac{1}{\rho}\sum_k\nabla\cdot(\rho h_k D_k\nabla Y_k)-\frac{1}{\rho}\sum_k q_k\dot{m}_k'''\end{aligned} \tag{9}$$

This equation can be rearranged as

$$c_p\frac{DT}{Dt}=\frac{1}{\rho}\nabla\cdot(k\nabla T)+\frac{1}{\rho}\sum_k\nabla\cdot(\rho h_k D_k\nabla Y_k)-\frac{1}{\rho}\sum_k(q_k+\xi_k)\dot{m}_k''' \tag{10}$$

where

$$c_p=\left.\frac{\partial h}{\partial T}\right|_{p_0,Y_k},\qquad \xi_k\equiv\left.\frac{\partial h}{\partial Y_k}\right|_{p_0,T,Y_{j,j\neq k}}\quad\text{and}\quad\frac{DY_k}{Dt}=\frac{1}{\rho}\dot{m}_k''' \tag{11}$$

For cases with mass transfer at the two-phase interface, the mass production rate is non-zero only in the source layer. Thus, $\xi_k=0$ and Eq. (10) becomes

$$\frac{\partial T}{\partial t}+\nabla\cdot(T\mathbf{u})=T\nabla\cdot\mathbf{u}+\frac{1}{\rho c_p}\nabla\cdot(k\nabla T)+\frac{1}{\rho c_p}\sum_k\nabla\cdot(\rho h_k D_k\nabla Y_k)-\frac{1}{c_p}\sum_k q_k\dot{m}_k''' \tag{12}$$

With the modeled volumetric source $\nabla\cdot\mathbf{u}=S_v$ and mass production rate $\dot{m}_k'''$, the energy equation can be solved with an explicit scheme. Substitution of Eq. (1) into (4) gives the species equation as follows:

$$\frac{\partial Y_k}{\partial t}+\nabla\cdot(Y_k\mathbf{u})=Y_k\nabla\cdot\mathbf{u}+\frac{1}{\rho}\nabla\cdot(\rho D_m\nabla Y_k)+\frac{1}{\rho}\dot{m}_k''' \tag{13}$$

This equation has a form similar to the energy equation (Eq. (12)) and can be solved by the same method.

The velocity divergence $\nabla\cdot\mathbf{u}$ due to thermal expansion in the gas phase can be obtained from the equation of state, in which the pressure p_0 is expressed as a function of density ρ, temperature T, and species mass fraction Y_k [12]. Taking the material derivative of the equation of state, we obtain

$$\frac{Dp_0}{Dt}=\frac{\partial p_0}{\partial\rho}\frac{D\rho}{Dt}+\frac{\partial p_0}{\partial T}\frac{DT}{Dt}+\sum_k\frac{\partial p_0}{\partial Y_k}\frac{DY_k}{Dt}=0 \tag{14}$$

Combination of this equation with the mass conservation equation, Eq. (1), gives rise to

$$\nabla\cdot\mathbf{u}=\left(\rho\frac{\partial p_0}{\partial\rho}\right)^{-1}\left(\frac{\partial p_0}{\partial T}\frac{DT}{Dt}+\sum_k\frac{\partial p_0}{\partial Y_k}\frac{DY_k}{Dt}\right) \tag{15}$$

For flows without chemical reactions, the velocity divergence reduces to

$$\nabla\cdot\mathbf{u}=\left(\rho\frac{\partial p_0}{\partial\rho}\right)^{-1}\left(\frac{\partial p_0}{\partial T}\frac{1}{\rho c_p}\nabla\cdot(k\nabla T)+\sum_k\frac{\partial p_0}{\partial Y_k}\frac{1}{\rho}\nabla\cdot(\rho D_m\nabla Y_k)\right) \tag{16}$$

With the ideal gas assumption, the equation of state can be written as:

$$p_0=\frac{\rho R_u T}{\overline{M}}=\frac{\rho R_u T}{\sum_k X_k M_k} \tag{17}$$

where R_u is the universal gas constant, X_k the mole fraction of species k, M_k the molecular weight of species k, and $\overline{M}$ the molar averaged molecular weight. Substitution of Eq. (17) into Eq. (16) yields

$$\nabla\cdot\mathbf{u}=(\rho c_p T)^{-1}\nabla\cdot(k\nabla T) \tag{18}$$

Equation (18) relates the velocity divergence to the spatial temperature distribution in the gas phase and is treated as the volume source in the momentum, energy, and species equations.

For the liquid phase, we assume that the density ρ is solely determined by temperature T. The velocity divergence $\nabla\cdot\mathbf{u}$ due to thermal expansion is written as

$$\nabla\cdot\mathbf{u}=-\frac{1}{\rho}\frac{D\rho(T)}{Dt}=-\frac{1}{\rho}\frac{D\rho}{DT}\frac{DT}{Dt} \tag{19}$$

The material derivative of temperature in the liquid phase can be acquired from the general form of the temperature derivative (Eq. (10)) with $Y_k=1$ and $m_k'''=0$,

$$\frac{DT}{Dt}=\frac{1}{\rho c_p}\nabla\cdot(k\nabla T) \tag{20}$$

Substitution of Eq. (20) into Eq. (19) gives the velocity divergence due to thermal expansion in the liquid phase,

$$\nabla\cdot\mathbf{u}=-\frac{1}{\rho^2 c_p}\frac{D\rho}{DT}\nabla\cdot(k\nabla T) \tag{21}$$

In the present work, the VOF approach is used to capture the time-evolving two-phase interface. The transport equation for volume fraction reads

$$\frac{\partial F}{\partial t}+\mathbf{u}\cdot\nabla F=0 \tag{22}$$

where F is the liquid volume fraction in grid cells. $F=1$ in the liquid phase and $F=0$ in the gas phase.

Equations (5), (6), (12), (13), (18), (21), (22) constitute the system of governing equations for two-phase flows with mass and energy transfer in the low-Mach limit. The formulation, however, remains unclosed, because of the lack of a vaporization model for the two-phase interface, which will be discussed in the following section.

3. Heat and mass transfer at the interface

At the interface, we employ the heat and mass transfer model based on the decomposed mechanisms proposed by Wang and Yang [1], which has demonstrated great accuracy and efficiency in dealing with liquid vaporization with large deformation. In this model, as shown in Fig. 1, the mass transfer and consequent change of normal velocity at the interface is expanded over a banded region of finite thickness across the interface. The banded region includes a source layer with positive mass production rate $\dot{m}'''$ on the gas side to model the increments of volume, mass, and energy due to vaporization, and a sink layer with negative mass production rate $\dot{m}'''$ on the liquid side to model the loss of volume, mass and energy. The corresponding thicknesses are denoted by δ_{source} and δ_{sink}, respectively. Each layer covers an appropriate number of grid cells. The distances of the central surfaces of the source and sink layers from the interface are denoted by d_{source} and d_{sink}, respectively. The numerical grids near the interface are sufficiently dense to resolve both the source and sink layers as well as the region between the two layers. The velocity divergence in the gas and liquid phases due to mass transfer is described by

$$\nabla\cdot\mathbf{u}=\frac{\dot{m}'''}{\rho} \tag{23}$$

The negative mass production rate ($\dot{m}_{sink}'''<0$) in the sink layer creates an additional normal velocity toward the liquid phase for fluid outside the sink layer. It pulls the two-phase interface to the liquid phase to model the interfacial regression. In the meantime, the positive mass production rate ($\dot{m}_{source}'''>0$) in the source layer causes an increase in normal velocity in the

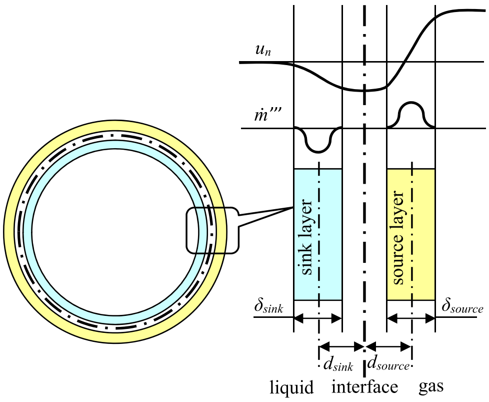

Fig. 1. Vaporization model based on decomposed mechanisms [1].

gas phase to account for the Stefan flow that takes place in the course of vaporization. The mass conservation in the liquid phase ensures that the interfacial regression is consistent with the mass transfer rate due to vaporization. In the region between the source and sink layers, the velocity varies continuously across the interface, and this guarantees the accuracy of interface localization with any well-developed method for two-phase flows without mass transfer.

The continuous mass production in the source and sink layers relates to the mass vaporization rate as,

$$\int\limits_{\delta_{source}} \dot{m}'''_{source} dx = -\int\limits_{\delta_{sink}} \dot{m}'''_{sink} dx = \dot{m}'', \tag{24}$$

where x is the coordinate normal to the interface with the origin at the center of each layer. $\dot{m}''$ is the surface vaporization rate in mass determined by the net heat flux to the interface,

$$\dot{m}'' = \frac{1}{\Delta h_{fg}} \left(k_{gas} \left.\frac{\partial T}{\partial n}\right|_{s,g} - k_{liquid} \left.\frac{\partial T}{\partial n}\right|_{s,l} \right) \tag{25}$$

where Δh_{fg} is the enthalpy of vaporization. A sinusoidal profile is adopted to describe the mass production rate in the source and sink layers,

$$\begin{cases} \dot{m}'''_{source} = \dfrac{\dot{m}''}{\delta_{source}} (1 + \cos(2\pi x/\delta_{source})) \\ \dot{m}'''_{sink} = -\dfrac{\dot{m}''}{\delta_{sink}} (1 + \cos(2\pi x/\delta_{sink})) \end{cases} \tag{26}$$

As a consequence of the interface curvature as well as the deviation of the source and sink layers from the interface, the areas of the central surfaces of the source and sink layers are different from that of the interface. This causes errors in the numerical calculation of the mass transfer rate. Here we introduce two correction factors for the mass production rates in the source and sink layers to compensate for the area change of the two layers,

$$\dot{m}''_{source} \equiv \alpha_{source} \dot{m}'' \quad \text{and} \quad \dot{m}''_{sink} \equiv \alpha_{sink} \dot{m}'' \tag{27}$$

and

$$\begin{aligned} \alpha_{source} &= \frac{\Delta S_{interface}}{\Delta S_{source}} = \frac{R_{curv}^2}{(R_{curv} + d_{source})^2} \\ \alpha_{sink} &= \frac{\Delta S_{interface}}{\Delta S_{sink}} = \frac{R_{curv}^2}{(R_{curv} - d_{sink})^2}, \end{aligned} \tag{28}$$

where d_{source} and d_{sink} are the distances of the center surfaces of the source and sink layers from the interface, respectively, and R_{curv} the radius of the interface curvature.

The energy equation (Eq. (3)) and the species mass fraction equation (Eq. (4)) are coupled through the surface vaporization equation (Eq. (25)). The surface temperature T_s is also affected by the vapor pressure at the interface according to the

Clausius-Clapeyron equation,

$$\ln \frac{p_{vapor,s}}{p} = \frac{\Delta h_{fg} M_{vapor}}{R_u}\left(\frac{1}{T_{boil}} - \frac{1}{T_s}\right) \tag{29}$$

where $p_{vapor,s}$ is the partial pressure of vapor at the interface, p the total pressure, M_{vapor} the molecular weight of the vapor species, and R_u the universal gas constant. This condition makes the interface temperature T_s slightly below the boiling temperature T_{boil}, a situation commonly known as the pseudo wet-bulb state [23]. The vapor partial pressure $p_{vapor,s}$ is related to the vapor mole fraction $X_{vapor,s}$ as $X_{vapor,s} = p_{vapor,s}/p$. Substitution of this expression into the Clausius-Clapeyron equation (Eq. (29)) provides another link between the energy and species balances,

$$\ln X_{vapor,s} = \frac{\Delta h_{fg} M_{vapor}}{R_u}\left(\frac{1}{T_{boil}} - \frac{1}{T_s}\right) \tag{30}$$

Physically, the vapor mole fraction at the two-phase interface $X_{vapor,s}$ depends on the surface vaporization rate $\dot{m}''$ and the species transport described by Eq. (4). At the same time, $X_{vapor,s}$ couples with T_s through the Clausius-Clapeyron equation. The energy equation (Eq. (3)) and the mass-fraction equation (Eq. (4)), as well as the links between them, that is, the surface vaporization equation (Eq. (25)) and the Clausius-Clapeyron equation (Eq. (29)), constitute the formulation of liquid vaporization.

4. Numerical method

The present work incorporates the vaporization model into the well-developed VOF-based code Gerris, which was initially developed for multiphase incompressible flows. In Gerris, the governing equations are solved by the numerical method proposed by Popinet [20,21], which combines quad/octree discretization, a time-staggered projection method, and a multilevel Poisson solver. We extend the application range of Gerris to situations with density variations in both the gas and liquid phases. The non-zero velocity divergence is taken into account by adding a source term to the right-hand-side of the Poisson equation. All the effects related to the volume dilatation and fluid property variations are treated as the source terms in the transport equations. The liquid density is determined solely by the local temperature, while the gas density depends on the species composition and temperature, as follows.

$$\rho = \begin{cases} \rho_{liquid}(T), & \text{liquid phase} \\ p_0 \sum_k M_k / R_u T, & \text{gas phase} \end{cases} \tag{31}$$

The time-staggered projection method is used to solve the flow equations,

$$\begin{aligned} &\rho^{n+1/2}\mathbf{u}^* - \Delta t \nabla\cdot\left(\mu^{n+1/2}\mathbf{D}^*\right) \\ &\quad = \Delta t\nabla\cdot\left(\mu^{n+1/2}\mathbf{D}^n\right) + \Delta t(\sigma\kappa\delta_s\mathbf{n})^{n+1/2} + \rho^{n+1/2}\mathbf{u}^n - \Delta t\rho^{n+1/2}\mathbf{u}^{n+1/2}\cdot\nabla\mathbf{u}^{n+1/2} \end{aligned} \tag{32}$$

$$\nabla\cdot\left(\frac{\Delta t}{\rho^{n+1/2}}\nabla p^{n+1/2}\right) = \nabla\cdot\mathbf{u}^* - S_v^{n+1/2} \tag{33}$$

$$\mathbf{u}^{n+1} = \mathbf{u}^* - \frac{\Delta t}{\rho^{n+1/2}}\nabla p_g^{n+1/2} \tag{34}$$

The volume source S_v^{n+1} results from the divergence of $\mathbf{u}^{n+1}$. It is determined by Eq. (18) in the gas phase and Eq. (21) in the liquid phase, respectively, and Eq. (23) in the source and sink layers.

The transport equations for temperature and mass fraction are discretized by an explicit scheme at each time level.

$$\begin{aligned} T^{n+1/2} &= T^{n-1/2} - \Delta t\nabla\cdot\left(T^n\mathbf{u}^n\right) + \Delta t T^n\nabla\cdot\mathbf{u}^n + \frac{\Delta t}{\rho^n c_p^n}\nabla\cdot\left(k^n\nabla T^n\right) \\ &\quad + \frac{\Delta t}{\rho^n c_p^n}\sum_k \nabla\cdot\left(\rho^n h_k^n D_k^n \nabla Y_k^n\right) - \frac{\Delta t}{c_p^n}\sum_k q_k \dot{m}_k''' \end{aligned} \tag{35}$$

$$Y_{vapor}^{n+1/2} = Y_{vapor}^{n-1/2} - \Delta t\nabla\cdot\left(Y_{vapor}^n\mathbf{u}^n\right) + \Delta t Y_{vapor}^n\nabla\cdot\mathbf{u}^n + \frac{\Delta t}{\rho^n}\nabla\cdot\left(\rho^n D_m^n\nabla Y_{vapor}^n\right) + \frac{\Delta t}{\rho^n}\dot{m}_{vapor}''' \tag{36}$$

The transport equation for volume of fluid is also discretized by an explicit scheme.

$$F^{n+1/2} = F^{n-1/2} - \Delta t\mathbf{u}^n\cdot\nabla F^n \tag{37}$$

The spatial discretization of Eqs. (32)–(37) is realized through a graded quadtree partitioning. The details are given in Refs. [20,21].

Table 1
Properties of n-decane and air at 1 atm.

	ρ (kg/m^3)	υ (m^2/s)	k (kJ/s m k)	c_p (kJ/kg K)
liquid n-decane at 447 K	604.14	3.35×10^{-7}	9.49×10^{-5}	2.81
vapor n-decane at 447 K	4.13	1.86×10^{-6}	2.14×10^{-5}	2.35
vapor n-decane at 1000 K	1.80	9.72×10^{-6}	8.10×10^{-5}	3.74
air at 447 K	0.789	3.17×10^{-5}	3.66×10^{-5}	1.02
air at 1000 K	0.353	1.23×10^{-4}	6.77×10^{-5}	1.14

The volume-based thermal properties of the gas mixture are estimated by the molar-weighted average of the properties of each individual species as

$$A_{mix} = \sum_k X_k A_k \tag{38}$$

The mass-based thermal properties of the mixture, such as the specific heat capacity, are estimated by the mass-weighted average of the properties of each individual species,

$$B_{mix} = \sum_k Y_k B_k \tag{39}$$

5. Model verification and validation

Considerable verification and validation has been performed on the Gerris code for flows without mass transfer. The code has demonstrated its capability, robustness, and accuracy in dealing with multiphase flows with strong liquid deformation [24–26]. In the present work, the model verification and validation is focused on flows with large liquid/gas density ratios and high vaporization rates combined with strong liquid deformation. The major challenges of this kind of flow simulation result from the low interface regression rate compared with the high velocity jump across the interface, and the strong coupling of thermal and mass transfer near the interface. In this section, several test cases are considered to demonstrate the efficient implementation and reliable solution of the present approach.

The experiment of Wong and Lin [27] provides temporally-resolved measurements of the size and temperature of an n-decane droplet in air, allowing for direct validation of the present model under high vaporization conditions. In their experiment, a spherical droplet with an initial diameter $D_0 = 1.98$ mm and initial temperature $T_{d,0} = 315$ K was suspended in a hot air flow with $T_{\text{air}} = 1000$ K and $U_{\text{air}} = 1$ m/s at one atmosphere. The corresponding boiling temperature of n-decane is 447 K. Table 1 lists the properties of n-decane and air at various temperatures.

The binary diffusion coefficient of n-decane vapor in air is given as follows [28]

$$D_m = \frac{3}{16}\frac{(4\pi k_B T/M w_{AB})^{1/2}}{(p/R_u T)\pi\sigma_{AB}^2 \Omega_D} f_D \propto \frac{T^{3/2}}{p} \tag{40}$$

We obtain $D_m = 2.2 \times 10^{-5}$ m^2/s at 1 atm and 273 K. In general, D_m can be estimated by the following equation.

$$D_m = 2.2 \times 10^{-5} \times \left(\frac{T}{273}\right)^{3/2} \times \left(\frac{1}{p}\right) \tag{41}$$

where the unit of p is atm. The surface tension of liquid n-decane is a function of temperature [29]

$$\sigma = 0.112 \times \left(1 - \frac{T}{647.3}\right)^{0.71} \text{ kg/s}^2 \tag{42}$$

Under the conditions considered in this study, the droplet remains axisymmetric about the centerline. The conservation equations of mass, momentum, energy and species in the axisymmetric form are thus solved on the meridian plane. In the simulation, the thickness of the source and sink layers is taken to be $\delta_{source} = \delta_{sink} = 1/35 R_{d,0}$, and the distance of the layers from the interface is $d_{source} = d_{sink} = 1/20 R_{d,0}$, where $R_{d,0}$ is the initial droplet radius. Technically, the smaller the layer thickness $\delta_{source\ \&\ sink}$ and the smaller the layer distance $d_{source\ \&\ sink}$, the closer the model is to the real mechanisms. We compared the temperature gradients at the interface between two separate simulations with $\delta_{source\ \&\ sink} = 1/35 R_{d,0}$, $d_{source\ \&\ sink} = 1/20 R_{d,0}$ and $\delta_{source\ \&\ sink} = 1/18 R_{d,0}$, $d_{source\ \&\ sink} = 1/10 R_{d,0}$. The relative difference is less than 3%. The selection of $\delta_{source\ \&\ sink}$ and $d_{source\ \&\ sink}$ is primarily determined by the accuracy requirement of the specific work.

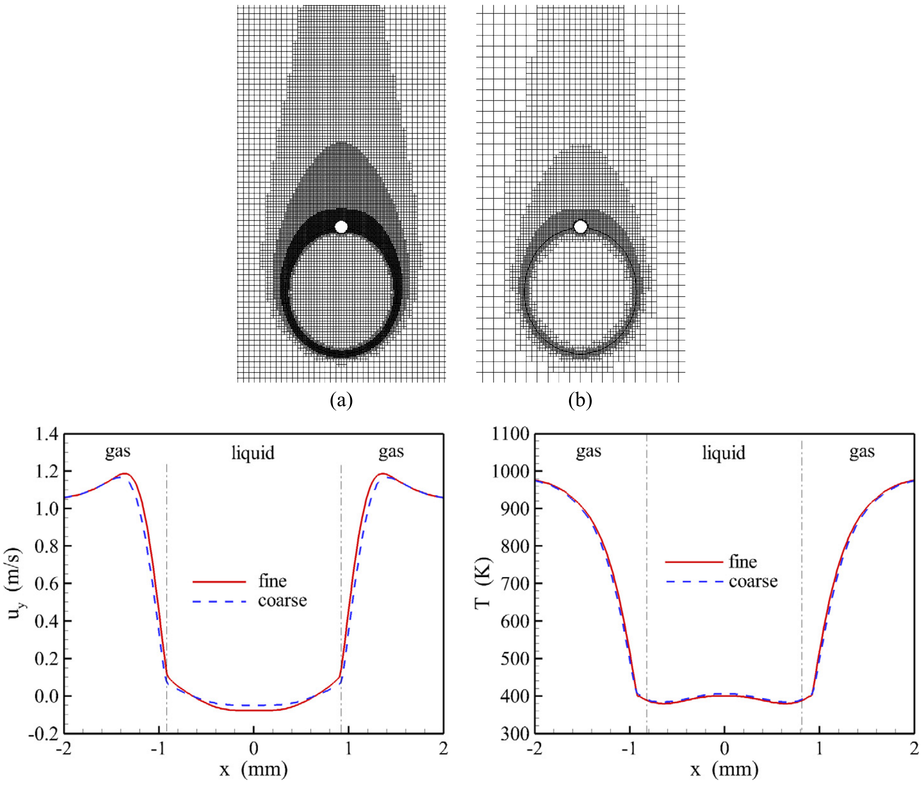

(c) (d)

Fig. 2. Effect of grid resolution on streamwise velocity and temperature for vaporization of suspended n-decane droplet in uniform airflow at $t = 2$ s (a) fine grid with $\Delta_{\min} = 0.01R_0$; (b) coarse grid with $\Delta_{\min} = 0.02R_0$; (c) streamwise velocity and (d) temperature on cross section through droplet center.

5.1. Grid independence study

An adaptive mesh refinement algorithm is used to dynamically resolve the flow characteristics according to the spatial gradients of temperature and vapor mass fraction. To examine the grid sensitivity of the numerical result, simulations were conducted with two different sets of grids: a fine grid with $\Delta_{\min} = 0.01R_{d,0}$ and a coarse grid with $\Delta_{\min} = 0.02R_{d,0}$, where $\Delta_{\min}$ is the minimum grid size and $R_{d,0}$ is the initial droplet radius. The total numbers of node points for the coarse and fine grids are roughly 5000 and 11000, respectively. Fig. 2 shows a comparison of the results and the corresponding distributions of streamwise velocity and temperature at $t = 2$ s. At each level of controlling variables, that is, spatial gradients of temperature and vapor mass fraction, the size of the coarse grid is twice that of the fine grid. Figs. 2(c) and 2(d) show the distributions on the cross section through the droplet center. Excellent convergence from the coarse to the fine grids is obtained. Nevertheless, the fine grid is used for all cases in the present study to ensure the numerical accuracy. Detailed flow and temperature structures will be discussed in Section 5.4.

5.2. Thermal expansion of quiescent n-decane droplet with constant surface temperature

Thermal expansion of the liquid phase caused by density variation is considered. To verify the model, we examine the mass variation of a quiescent n-decane droplet heated with constant surface temperature $T_s = T_{boil} = 447$ K. The initial droplet temperature is $T_{d,0} = 315$ K, and the droplet diameter is $D_0 = 1.98$ mm. For testing purposes, mass transfer across the droplet surface is not treated. The liquid density is taken to be a linear function of temperature.

$$\rho = a + bT \tag{43}$$

For liquid n-decane, $\rho = 713.43$ kg/m^3 at $T = 315$ K and $\rho = 604.14$ kg/m^3 at $T = 447$ K, giving $a = 974.26$ kg/m^3, $b = -0.828$ kg/(m^3 K). The velocity divergence in the liquid phase can be acquired by substituting Eq. (43) into Eq. (21).

In the heating process, the droplet size increases as the density decreases, yet the droplet mass remains constant. Fig. 3(a) shows the temporal evolution of the temperature profile in the droplet. The ratios of the droplet mass and volume to their initial values are presented in Fig. 3(b). The mass ratio $m_d/m_{d,0}$ remains at unity throughout the heating period. The volume ratio $V_d/V_{d,0}$ increases from unity at $t = 0$ s and asymptotically approaches the analytical value of $V_d/V_{d,0} = 1.18$

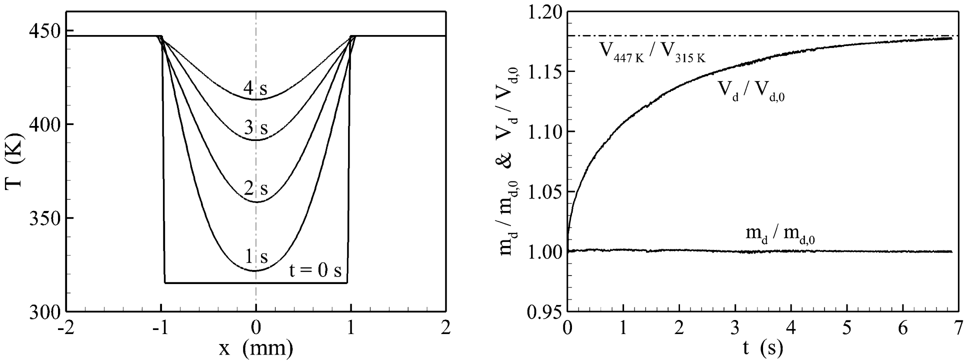

(a) (b)

Fig. 3. Temporal evolution of (a) temperature distribution and (b) relative mass and volume of an n-decane droplet without vaporization. $T_{d,0} = 315$ K, $T_s = 447$ K, $D_0 = 1.98$ mm.

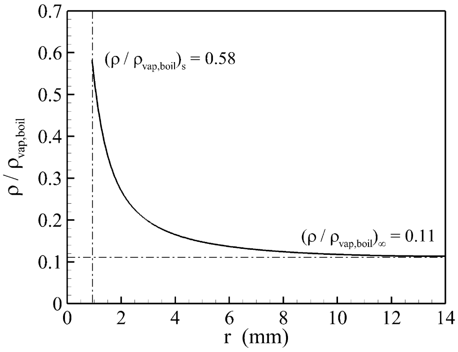

Fig. 4. Radial distribution of density ratio.

at $T_d = 447$ K. This validation case ensures accurate treatment of volume variation and guarantees mass conservation in the heating process.

5.3. Vaporization of *n*-decane droplet in quiescent air

As part of the model validation, we examine the vaporization of a single n-decane droplet in quiescent air and validate the present model against the classical D^2 law [28]. With the assumption of uniform properties and quasi-steady-state conditions, the conservation equations of mass and energy can be solved analytically [28], giving the evolution of the droplet diameter in the following form,

$$D^2 = D_0^2 - Kt \tag{44}$$

where the constant K can be determined by the fluid properties estimated at the reference temperature and mass fraction.

Fig. 4 shows the calculated density field in the gas phase. Roughly 13000 numerical grids are used on the meridian plane. The gas density decreases from $(\rho/\rho_{vapor,boil})_s = 0.58$ at the droplet surface to 0.11 in the far field. Fig. 5 shows the temporal evolution of the square of the droplet diameter predicted by the numerical and analytical methods. Two different methods were used to calculate the droplet diameter in the numerical simulation. The first is based on the volume of the liquid phase, and the second involves the subtraction of the liquid volume of the evaporated liquid in the gas phase from the initial liquid volume. The comparison allows for examination of the consistency between the mass of the evaporated liquid and that of the lost liquid. The mass of the evaporated liquid is calculated by

$$m_{vapor} = \int\limits_{V_{gas}} \rho_{gas} Y_{vapor} dV_{gas} \tag{45}$$

For variable-density flows with sharp changes of temperature and species concentration across the interface, it is a challenge to accurately estimate the fuel vapor mass. The numerically predicted diameter square D^2 estimated with the two methods agrees fairly well with the analytical result. In the early stage ($t < 0.5$ s), the slopes of the numerical results are slightly larger than that of the analytical prediction. This is caused by the use of $Y_{vapor} = 0$ and $T_{gas} = 1000$ K as the initial condition

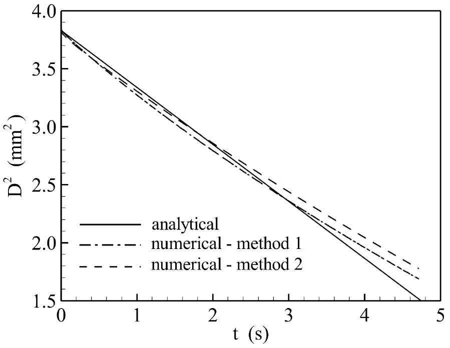

Fig. 5. Temporal evolution of square of n-decane droplet diameter in quiescent air ($T_{\mathrm{air}} = 1000$ K).

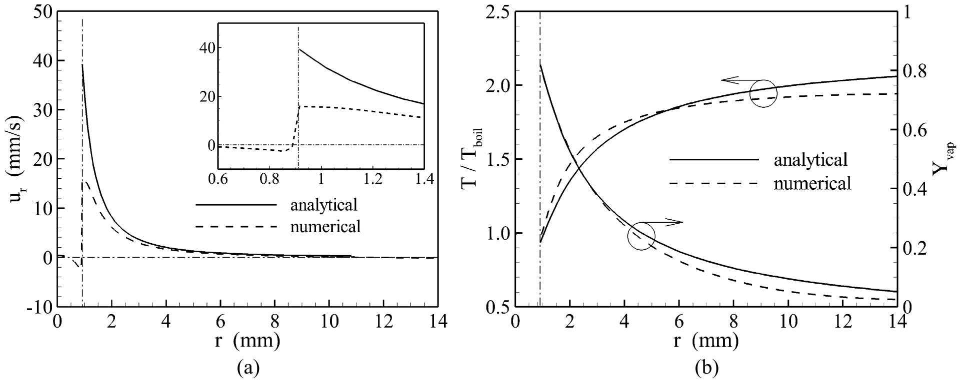

(a)

(b)

Fig. 6. Numerical and analytical results at $t = 1$ s for n-decane droplet vaporization in quiescent air: (a) distribution of radial velocity; (b) distributions of temperature and vapor mass fraction.

in the numerical simulation. The temperature and species fields undergo an initial transient process. The analytical solution, however, assumes that the temperature and species concentrations obey the quasi-steady distribution. In the fully developed stage ($t > 0.5$ s), the slopes of the numerical results are smaller than their analytical counterpart. Deviation primarily results from the constant-density assumption in the analytical model. The figure also shows that the numerically predicted D^2 of the two methods agree well in terms of droplet regression rate, (dD^2/dt) except in the initial range ($t < 1$ s), in which Method 2 slightly under-estimates the prediction by Method 1. This is attributed to the establishment of vapor concentration in the source layer in the initial period.

Fig. 6 shows the distributions of radial velocity, temperature, and mass fraction in the gas phase at $t = 1$ s. The continuous vaporization creates a Stefan flow in the gas phase; the velocity of the Stefan flow obeys mass conservation in the spherical coordinate system. As shown in Fig. 6(a), the calculated radial velocity is smaller than the analytical prediction near the interface. The difference is caused by the constant-density assumption applied by the analytical solution. The gas density near the interface is under-estimated by the analytical solution, rendering a larger radial velocity as compared with the numerical solution. Fig. 6(b) shows the normalized temperature and fuel vapor mass fraction in the gas phase. At the droplet surface, the numerically predicted temperature is $(T_s/T_{boil})_{num} = 0.936$, which is slightly (0.11%) higher than the analytical value of $(T_s/T_{boil})_{anal} = 0.935$. The numerically predicted fuel vapor mass fraction at the droplet surface is $(Y_{vapor})_{num} = 0.821$, which is higher than the analytical prediction of $(Y_{vapor})_{anal} = 0.820$ by 0.12%. Both the temperature and vapor mass fraction of the numerical solution indicate noticeable deviation from the analytical prediction. Two reasons contribute to this phenomenon. First, the analytical model employs a quasi-steady assumption, for which the time scale for interface regression is much larger than for heat and mass transfer, a situation not well satisfied in the present study. Second, the analytical analysis ignores density variations in the gas and liquid phases.

5.4. Vaporization of n-decane droplet in uniform air flow

For a droplet vaporizing in a convective environment, the ambient gas flow interacts with the droplet and creates a boundary layer on the droplet surface. The heat and mass transfer between the liquid and gas phases are thus enhanced. Here the vaporization of an n-decane droplet in a hot, uniform air flow at 1 atm is treated, simulating the experiment of Wong and Lin [27]. The air flow velocity is $U_{gas} = 1$ m/s. The Reynolds number based on the initial droplet diameter and

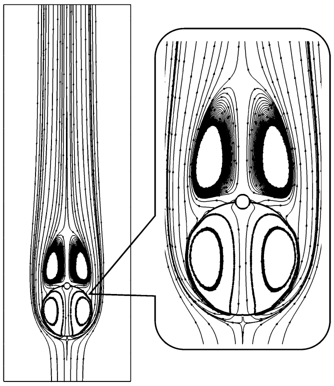

Fig. 7. Flow pattern of *n*-decane droplet suspended in uniform air flow at $t = 2$ s, $U_{\text{air}} = 1$ m/s and $T_{\text{air}} = 1000$ K.

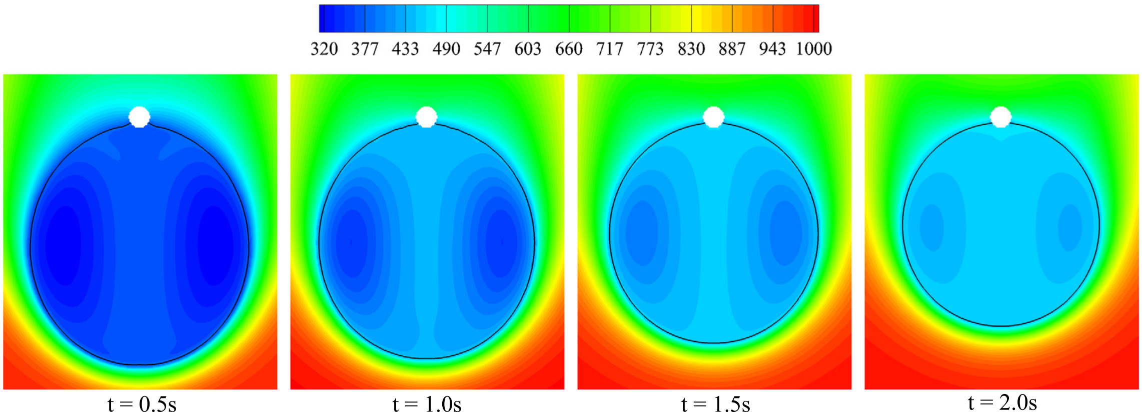

Fig. 8. Temporal variation of temperature inside *n*-decane droplet suspended in uniform air flow at $U_{\text{air}} = 1$ m/s and $T_{\text{air}} = 1000$ K.

air velocity is $\text{Re}_d = U_{gas} D_0 / \bar{\upsilon}_{gas} = 42.9$, where $\bar{\upsilon}_{gas}$ is the kinematic viscosity of the gas estimated with the 1/3 rule. The droplet basically remains spherical throughout its lifetime. In the simulation, the total number of numerical grids is roughly 11000 on the meridian plane.

Fig. 7 shows the flow pattern at $t = 2$ s. The droplet interior is characterized by an axisymmetric recirculating flow, which transfers heat from the droplet surface to the interior. Outside of the droplet, the Stefan flow created by the evaporated liquid forms an envelope around the droplet and separates the outer airflow from the droplet. The interface between the outer airflow and the inner Stefan flow provides space for chemical reactions in cases with liquid fuel combustion. As shown in the figure, an axisymmetric vortex bubble is generated in the wake of the droplet. The bubble does not appear in the flow predicted by the constant-density model under the same condition [1]. This difference is caused by the fact that the constant-density model underestimates the gas density near the interface, as shown in Fig. 4. It leads to a nonphysically higher vapor velocity and suppresses the vortex bubble in the wake of the droplet. The constant-density model fails to capture some salient flow characteristics related to the density variation and thermal expansion in the gas phase.

The droplet, which is initially at a low temperature, is first heated by the ambient hot air. At this stage, the heat from the hot air is mostly transferred to the droplet interior, and the interface temperature T_s and the vaporization rate $\dot{m}''$ are relatively low. Fig. 8 shows the temperature evolution in the droplet from $t = 0.5$ to 2.0 s. A small fraction of the heat transferred to the droplet goes to evaporate liquid to vapor, and the remainder is absorbed by the droplet and increases its interior temperature. The recirculating flow within the droplet acquires heat from the interface through diffusion, and then advects the heat to the interior.

As the droplet temperature increases, the heat transfer to the droplet interior is reduced, and the vaporization rate $\dot{m}''$ increases. Fig. 9 shows snapshots of the temperature T, vapor mass fraction Y_{vapor} and density ratio $\rho/\rho_{vapor,boil}$ fields at $t = 2$ s. The thermal and species boundary layers in which temperature and vapor mass fraction changes considerably are clearly identified. The region with lower temperature and higher vapor concentration extends downstream of the droplet due to the convection effect. Compared with the constant-density model [1], the droplet wake region with lower temperature and higher vapor mass fraction becomes wider because of the formation of the wake bubble. The gas density also varies around the droplet.

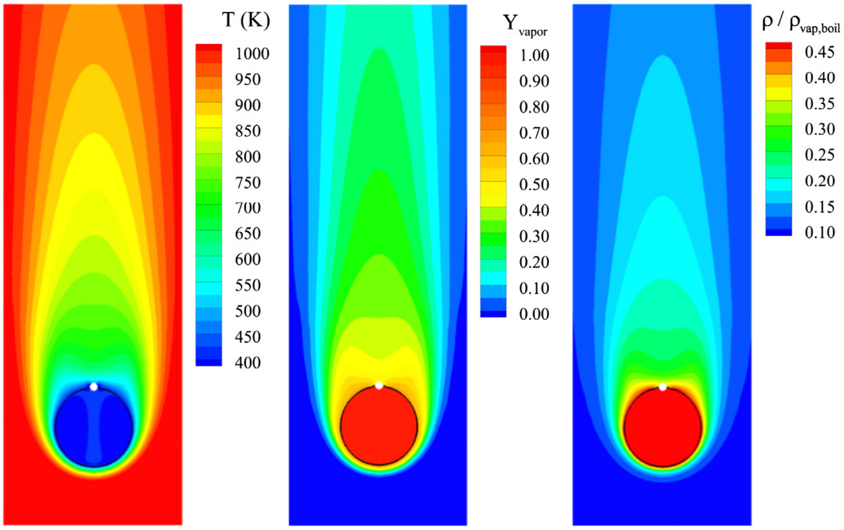

(a) (b) (c)

Fig. 9. Distributions of (a) temperature T, (b) vapor mass fraction Y_{vap} and (c) density ratio $\rho/\rho_{vap,boil}$, n-decane droplet suspended in uniform air flow at $U_{\text{air}} = 1$ m/s and $T_{\text{air}} = 1000$ K, $t = 2$ s.

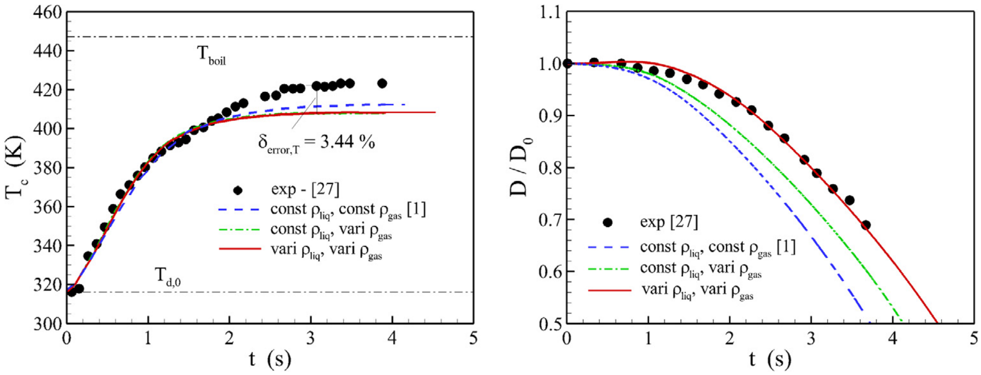

(a) (b)

Fig. 10. Temporal variations of (a) temperature at droplet center T_c, and (b) diameter D/D_0 for n-decane droplet suspended in uniform air flow, $U_{\text{air}} = 1$ m/s and $T_{\text{air}} = 1000$ K.

Fig. 10 compares the numerical prediction with the experimental measurement of Wong and Lin [27] in terms of the temporal variation of the droplet temperature and diameter. To distinguish the variable-density effects in the gas and liquid phases, we also include the two additional cases with (a) constant liquid density and variable gas density, and (b) constant liquid density and constant gas density [1]. The overall process can be divided into the droplet heating and vaporization stages. In the early period, the heat transferred to the droplet is mostly absorbed by the droplet, increasing the droplet temperature, and the vaporization rate is low. As the droplet heats up, the vaporization rate increases. Once the droplet surface temperature reaches its pseudo wet-bulb state, further heating is primarily consumed for phase change, and significant vaporization takes place.

Fig. 10(a) shows the temperature evolution at the droplet center, T_c. All the numerical predictions agree well with experimental data in the initial heating stage ($t < 1.7$ s). This is primarily because of the weak dependence of isobaric heat capacity (c_p) of liquid n-decane on temperature. When $t > 1.7$ s, the droplet temperature asymptotically approaches a constant value, and intense vaporization takes place. The final droplet temperatures predicted by the numerical models are lower than that of the experimental measurement. The relative error $\delta_{error,T} \equiv |T_{d,num} - T_{d,\text{exp}}|/T_{d,\text{exp}}$ of the numerical result in the variable gas-density case (with both constant and variable liquid density) is 3.44%. Such difference may be attributed to measurement uncertainty and/or the representation of the gas-liquid interface by finite-thickness source and sink layers. The latter can be improved by increasing the grid resolution and decreasing the thickness of the source/sink layers near the droplet surface.

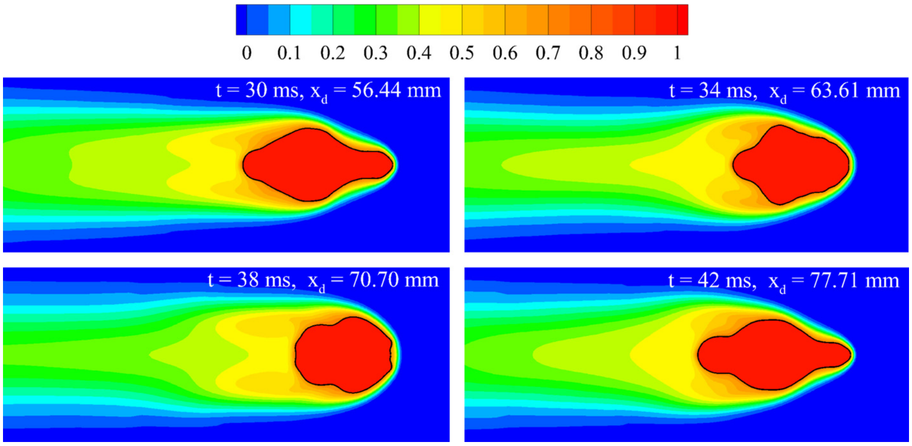

Fig. 11. Temporal evolution of vapor mass fraction for an impulsively started *n*-decane droplet in quiescent air, $U_0 = 2$ m/s.

Fig. 10(b) shows the temporal evolution of the droplet diameter. The result predicted by the present variable-density model agrees well with the experimental measurement over the entire lifetime of the droplet. The constant liquid-density assumption in the model, on the other hand, leads to premature droplet regression. The constant gas-density assumption further makes the droplet size reduction take place earlier. In the vaporization stage, the rate of droplet size reduction, $d(D/D_0)/dt$, measured by the curve slopes in the figure, are well predicted by the numerical models with either the constant or variable density treatment.

5.5. Vaporization of impulsively started n-decane droplet in quiescent air at 1 atm

In order to demonstrate the robustness of the present model, we study the vaporization of an impulsively started droplet in quiescent air. With the increase in the droplet initial velocity, the aerodynamic force exerted on the droplet gradually becomes stronger, leading to greater droplet deformation. When the velocity is large enough, droplet breakup takes place. Two non-dimensional parameters, the Weber and the Ohnesorge numbers, defined as $We = \rho_{gas} U_0^2 D_0/\sigma$ and $Oh = \mu_l/\sqrt{\rho_l D_0 \sigma}$, respectively, are identified to characterize droplet deformation and breakup. Here σ is the surface tension. General discussions of this subject can be found in Refs. [30,31].

At $t = 0$ s, an *n*-decane droplet with an initial diameter $D_0 = 1.98$ mm is placed in quiescent air with $T_{\text{air}} = 1000$ K. To focus on the vaporization of a deformed droplet, we ignore the heat transfer inside the droplet and assume that the droplet has been preheated to its final pseudo wet-bulb state when it starts to move. As a consequence of the interaction with the surrounding air, the droplet decelerates, deforms, and evaporates as it moves. The simulation covers a spatial domain of 0.2 m, about 100 times the droplet diameter. Two different initial droplet velocities $U_0 = 1$ and 2 m/s are considered. In the simulation with the constant-density model [1], modest deformation of the droplet occurs at $U_0 = 2$ m/s. In the present study with the variable-density model, the gas density near the droplet surface is relatively higher, facilitating droplet deformation through stronger aerodynamic force.

Fig. 11 shows the temporal evolution of droplet deformation and fuel vapor mass fraction for $U_0 = 2$ m/s. A total of 20000 numerical grids are used on the meridian plane in the calculation. The corresponding Weber number and Ohnesorge number are $We = 3.35$ and $Oh = 1.89 \times 10^{-3}$, respectively. According to the regime diagram of Hsiang and Faeth [30], droplet deformation in this case is subject to periodic oscillation, and this is consistent with the observation made in the present study.

Fig. 12 shows the temporal evolution of droplet position and diameter predicted by the constant-density and variable-density models. Here D is the equivalent diameter of a spherical droplet with the same volume. For the cases with the variable-density model, the droplet is surrounded by hot air with density relatively smaller than that of the constant-density model [1] in the far field, so the droplet velocity predicted by the variable-density model is slightly higher than that of the constant-density model for $U_0 = 1$ m/s. For $U_0 = 2$ m/s, the droplet deformation takes place when the variable-density model is employed. The drag force on the droplet becomes greater, making the droplet velocity smaller than that predicted by the constant-density model. The temporal variation of the droplet diameter shown in Fig. 12(b) indicates that the rate of diameter reduction, $d(D/D_0)/dt$, increases with increasing droplet velocity U_0. At $U_0 = 0$, the constant- and variable-density models provide almost the same result. At $U_0 > 0$, the difference between the two models arises. The rate of diameter reduction predicted by the variable-density model is smaller than its constant-density counterpart, and the difference increases with increasing droplet velocity. One factor contributing to this phenomenon is the uniform-property assumption utilized by the constant-density model. No experimental or numerical studies of vaporization of the deforming droplet are available in the literature for comparison. The results of the present study quantitatively demonstrate the expected trend in the rate of droplet size reduction. The model can be effectively used to study two-phase flows with large deformation and high mass transfer rate.

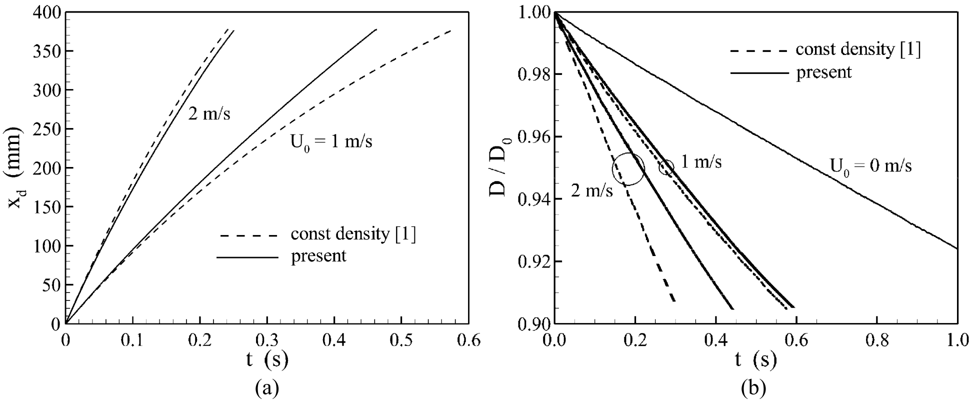

Fig. 12. Temporal evolution of droplet (a) position and (b) diameter for an impulsively started *n*-decane droplet in quiescent air at different initial velocities. Solid: present variable-density model; dashed: constant density model of Wang and Yang [1].

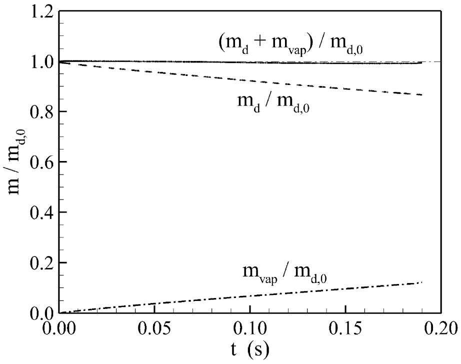

Fig. 13. Temporal evolution of liquid and fuel vapor mass, as well as their sum at $U_0 = 2$ m/s.

The conservation of liquid and vapor mass is closely examined over the droplet lifetime. Fig. 13 shows the temporal evolution of the liquid and vapor mass, as well as their sum at $U_0 = 2$ m/s. Here m_d and m_{vap} are the time-evolving droplet and fuel vapor mass, respectively, and $m_{d,0}$ the initial droplet mass. For an ideal case with perfect mass conservation, $(m_d + m_{vap})/m_{d,0}$ remains unity. As shown in the figure, the normalized vapor mass $m_{vap}/m_{d,0}$ increases from zero when the droplet starts to move. Correspondingly, the normalized droplet mass $m_d/m_{d,0}$ decreases from unity. The total fuel mass $(m_d + m_{vap})/m_{d,0}$ basically remains around unity. The relative error $|m_{d,0} - (m_d + m_{vap})|/m_{vap}$ is smaller than 0.05. The accuracy of the present vaporization model is validated in terms of mass conservation.

5.6. Vaporization of an impulsively started n-decane droplet at 10 atm

The vaporization of an impulsively started *n*-decane droplet in quiescent air at 10 atm is also studied to explore the effect of pressure on droplet behaviors. The initial droplet diameter is $D_0 = 0.1$ mm, and the starting velocity is $U_0 = 10$ m/s. The ambient air temperature is 1000 K. The heat transfer inside the droplet is ignored. Under this condition, the density ratio of liquid to gas is $\rho_{liquid}/\rho_{gas} = 52.65$, much larger than at 1 atm. The aerodynamic force on the droplet is so strong that large deformation of the droplet occurs. The Reynolds number is $\mathrm{Re}_d = 170.18$. The Weber number and Ohnesorge number are $We = 18.12$ and $Oh = 5.68 \times 10^{-3}$, respectively. The total number of numerical grids is roughly 20000 on the meridian plane. The droplet experiences the bag breakup mode under these conditions [30,31]. Fig. 14 shows the temporal evolution of the droplet deformation and the vapor mass-fraction field. A close-up view is given in Fig. 15. The solid line depicts the droplet surface. The deformation pattern observed resembles that seen by Han and Tryggvason [32] in similar parameter ranges. Liquid fuel evaporates from the droplet surface and forms a vortex ring in the wake of the droplet.

6. Conclusions

A novel vaporization model for liquids with large deformation and high mass transfer rate is developed. The formulation accommodates density and property variations in the flow field. The interfacial mass and heat transfer is treated by means

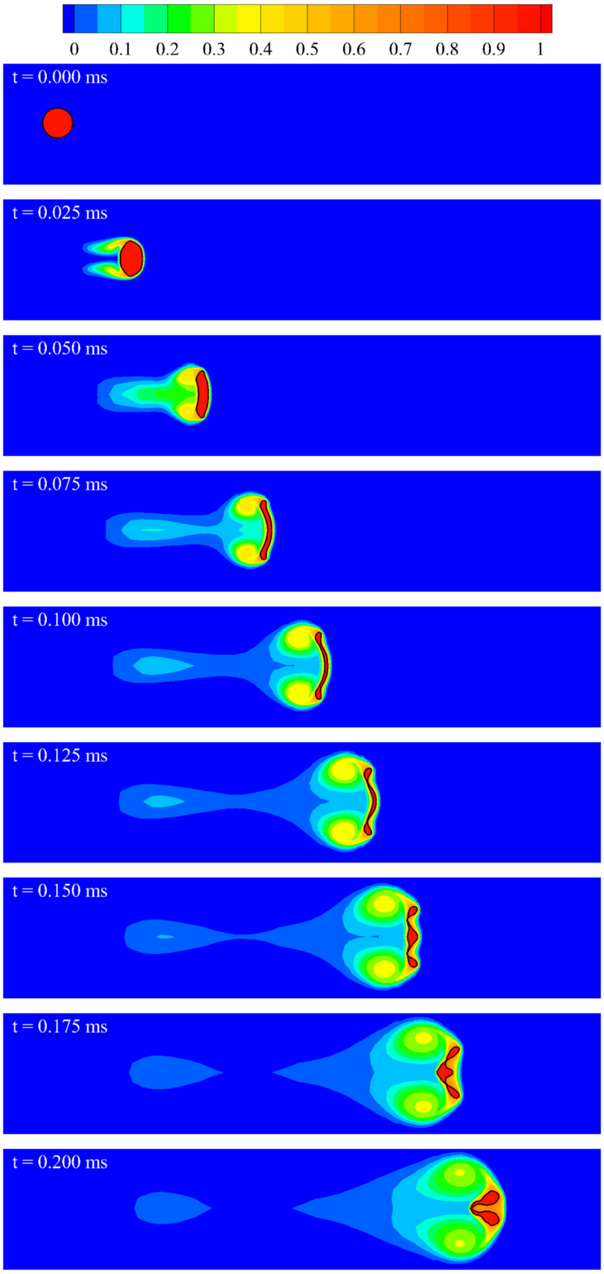

Fig. 14. Temporal evolution of vapor mass fraction for an impulsively started n-decane droplet in quiescent air, $D_0 = 0.1$ mm, $P_{\text{air}} = 10$ atm, $U_0 = 10$ m/s.

of two body-fitted source and sink layers with finite thickness in the gas and liquid phases, respectively, around the droplet surface. The approach can be effectively implemented in any well-developed interface localization method and circumvents the modeling and numerical difficulties caused by the combined treatment of mass/heat transfer and surface localization. The coupling of fully compressible gas phase and slightly compressible liquid phase is realized through a set of unified conservation equations in the low Mach number limit. The nonzero velocity divergence is treated as a source term in the conservation equations, and then solved by a modified projection method.

The vaporization model is not specific to the details of interface localization methods and can be incorporated into any of them. In this present study, it was implemented into the volume-of-fluid (VOF) based code Gerris, which was originally intended for flows with constant density and properties. As a model validation effort, a series of numerical simulations were conducted to study the vaporization of deforming droplets under various conditions. The model accuracy and robustness were carefully examined.

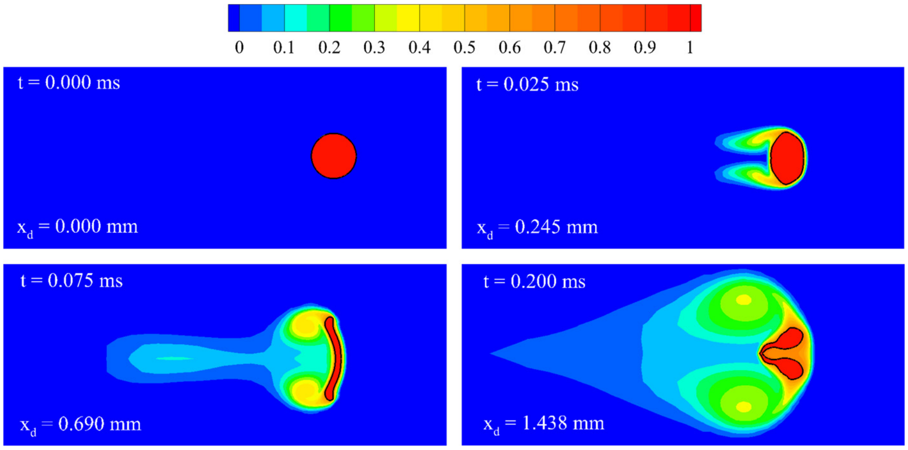

Fig. 15. Temporal evolution of vapor mass fraction for an impulsively started *n*-decane droplet in quiescent air, $D_0 = 0.1$ mm, $P_{air} = 10$ atm, $U_0 = 10$ m/s.

Acknowledgements

This work was partly sponsored by the US Army Research Office under the Multi-University Research Initiative under Contract No. W911NF-08-1-0124, and partly by the William R.T. Oakes Endowment of the Georgia Institute of Technology. Special thanks is due to Stéphane Popinet for allowing us to use his work on the VOF and AMR algorithms.

References

[1] Y. Wang, V. Yang, Vaporization of liquid droplet with large deformation and high mass transfer rate, I: constant-density, constant-property case, J. Comput. Phys. 392 (2019) 56–70, https://doi.org/10.1016/j.jcp.2019.03.013.
[2] G. Son, V.K. Dhir, Numerical simulation of film boiling near critical pressures with a level set method, J. Heat Transf. 120 (1998) 183–192.
[3] F. Gibou, L. Chen, D. Nguyen, S. Banerjee, A level set based sharp interface method for the multiphase incompressible Navier-Stokes equations, J. Comput. Phys. 222 (2007) 536–555.
[4] D. Juric, G. Tryggvason, Computations of boiling flows, Int. J. Multiph. Flow 24 (1998) 387–410.
[5] A. Esmaeeli, G. Tryggvason, Computations of film boiling. Part I: numerical method, Int. J. Heat Mass Transf. 47 (2004) 5451–5461.
[6] M. Ida, An improved unified solver for compressible and incompressible fluids involving free surfaces. Part I. Convection, Comput. Phys. Commun. 132 (2000) 44–65.
[7] M. Ida, An improved unified solver for compressible and incompressible fluids involving free surfaces. Part II. Multi-time-step integration and applications, Comput. Phys. Commun. 150 (2003) 300–322.
[8] R.W. Houim, K.K. Kuo, A ghost fluid method for compressible reacting flows with phase change, J. Comput. Phys. 235 (2013) 865–900.
[9] V. Yang, Modeling of supercritical vaporization, mixing, and combustion processes in liquid-fueled propulsion systems, Proc. Combust. Inst. 28 (2000) 925–942.
[10] H. Meng, G.C. Hsiao, V. Yang, J.S. Shuen, Transport and dynamics of liquid oxygen droplets in supercritical hydrogen streams, J. Fluid Mech. 527 (2005) 115–139.
[11] J.S. Shuen, V. Yang, C.C. Hsiao, Combustion of liquid-fuel droplets at supercritical conditions, Combust. Flame 89 (1992) 299–319.
[12] S.Y. Hsieh, V. Yang, A preconditioned flux-differencing scheme for chemically reacting flows at all Mach numbers, Int. J. Comput. Fluid Dyn. 8 (1997) 31–49.
[13] H. Meng, V. Yang, A unified treatment of general fluid thermodynamics and its application to a preconditioning scheme, J. Comput. Phys. 189 (2003) 277–304.
[14] R. Caiden, R.P. Fedkiw, C. Anderson, A numerical method for two-phase flow consisting of separate compressible and incompressible regions, J. Comput. Phys. 166 (2001) 1–27.
[15] M. Billaud, G. Gallice, B. Nkonga, A simple stabilized finite element method for solving two phase compressible-incompressible interface flows, Comput. Methods Appl. Mech. Eng. 200 (2011) 1272–1290.
[16] R.G. Rehm, H.R. Baum, The equations of motion for thermally driven, buoyant flows, J. Res. Natl. Bur. Stand. 83 (1978) 297–308.
[17] A. Majda, J. Sethian, The derivation and numerical solution of the equations for zero Mach number combustion, Combust. Sci. Technol. 42 (1985) 185–205.
[18] A.J. Chorin, A numerical method for solving incompressible viscous flow problems, J. Comput. Phys. 2 (1967) 12–26.
[19] P.A. McMurtry, W.H. Jou, J.J. Riley, R.W. Metcalfe, Direct numerical simulations of a reacting mixing layer with chemical heat release, AIAA J. 24 (1986) 962–970.
[20] S. Popinet, Gerris: a tree-based adaptive solver for the incompressible Euler equations in complex geometries, J. Comput. Phys. 190 (2003) 572–600.
[21] S. Popinet, An accurate adaptive solver for surface-tension-driven interfacial flows, J. Comput. Phys. 228 (2009) 5838–5866.
[22] J.B. Bell, M.S. Day, C.A. Rendleman, S.E. Woosley, M.A. Zingale, Adaptive low Mach number simulations of nuclear flame microphysics, J. Comput. Phys. 195 (2004) 677–694.
[23] K.C. Hsieh, J.S. Shuen, V. Yang, Droplet vaporization in high-pressure environments I: near critical conditions, Combust. Sci. Technol. 76 (1991) 111.
[24] X. Chen, D. Ma, V. Yang, S. Popinet, High-fidelity simulations of impinging jet atomization, At. Sprays 23 (2013) 1079–1101.
[25] X. Chen, V. Yang, Thickness-based adaptive mesh refinement methods for multi-phase flow simulations with thin regions, J. Comput. Phys. 269 (2014) 22–39.
[26] X. Chen, V. Yang, Recent advances in physical understanding and quantitative prediction of impinging jet dynamics and atomization, Chin. J. Aeronaut. 32 (2019) 45–57.
[27] S.C. Wong, A.C. Lin, Internal temperature distributions of droplets vaporizing in high-temperature convective flows, J. Fluid Mech. 237 (1992) 671–687.

[28] S.R. Turns, An Introduction to Combustion Concepts and Applications, McGraw-Hill, New York, 1996.
[29] C.C.M. Luijen, K.J. Bosschaart, M.E.H. van Dongen, High pressure nucleation in water/nitrogen systems, J. Chem. Phys. 106 (1997) 8116–8123.
[30] L.P. Hsiang, G.M. Faeth, Drop deformation and breakup due to shock wave and steady disturbances, Int. J. Multiph. Flow 21 (1995) 545–560.
[31] P. Khare, D. Ma, X. Chen, V. Yang, Phenomenology of Secondary Breakup of Newtonian Liquid Droplets, AIAA Paper 2012-0171, 2012.
[32] J. Han, G. Tryggvason, Secondary breakup of axisymmetric liquid drops. II. Impulsive acceleration, Phys. Fluids 13 (2001) 1554–1565.